Chapter 2 Instrumental and Experimental Methods

Atomic force microscopy (AFM) is a powerful tool to investigate the morphology and mechanical properties of protein nanotubes. In this chapter, the principles of AFM will be first introduced. Then the protocols of AFM analysis and image processing used in the later chapters will be explained. The preparation of protein nanotube samples for AFM analysis will also be presented.

2.1 Atomic Force Microscopy

2.1.1 Atomic Force Microscopy

AFM, which was invented in 1986, expanded the application of scanning tunnelling microscopy to nonconductive, soft, and live biological samples (Binnig *et al.* 1986; Zasadzinski *et al.* 1998; Marti *et al.*, 1998). AFM has several capabilities including the ability to characterize topographic details of surfaces from the submolecular to the cellular level (Radmacher *et al.* 1992), monitor the dynamic processes of single molecules in physiologically relevant solutions (Engell and Muller 2000), and measure the forces between interacting molecules (Zlatanova *et al.* 2000). AFM is a powerful tool for characterizing the structural properties of macromolecular complexes both in air and under near-physiological conditions. In addition, modified AFMs can be used to manipulate single

molecules (Yang *et al.* 2003). In the past two decades, the application of AFM has spread to many areas of biological sciences including studies of DNA (Fritzsche *et al.* 1997; Hansma 2001), RNA (Lyubchenko *et al.*1992; Bonin *et al.* 2000; Henn *et al.* 2001; Liphardt *et al.* 2001), proteins (Heymann *et al.* 1997; Isralewitz *et al.* 2001), lipids (Dufrene 2000; Balashev *et al.* 2001), carbohydrates (Misevic 1999; Dettmann *et al.* 2000; Marszalek *et al.* 2001), biomolecular complexes (Lyubchenko *et al.* 1995; Willemsen *et al.* 2000; Safinya 2001), organelles (Oberleithner *et al.*, 1997; Danker and Oberleithner 2000) and cells (Henderson 1994; Ohnesorge *et al.* 1997).

2.1.1.1 Principle of AFM

The principle of the AFM is relatively simple (**Figure 2-1**). The key element of the AFM is the cantilever. It consists of one or more beams of silicon or silicon nitride of 100–500 μm in length and 0.5–5 μm in thickness. At the end of the cantilever a sharp tip is mounted to sense the force acting between it and the sample surface. Photos of general purpose silicon nitride cantilevers (Veeco Probes, Camarillo, CA, USA) are shown in **Figure 2-2**. For normal topographic imaging, the tip is brought into continuous or intermittent contact with the sample as it raster-scans over the surface. An optical system is then used to measure the changes of the laser beam reflected from the gold-coated back of the cantilever onto a position-sensitive photodiode (PSPD), which can measure changes in the position of the incident laser as small as 0.1 nm.

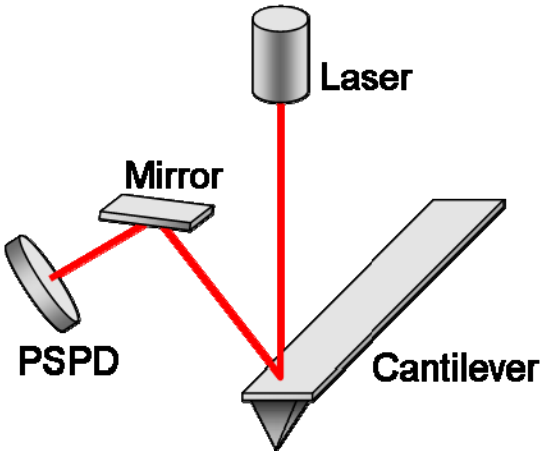

Figure 2-1 Schematic of the concept of AFM and the optical lever.

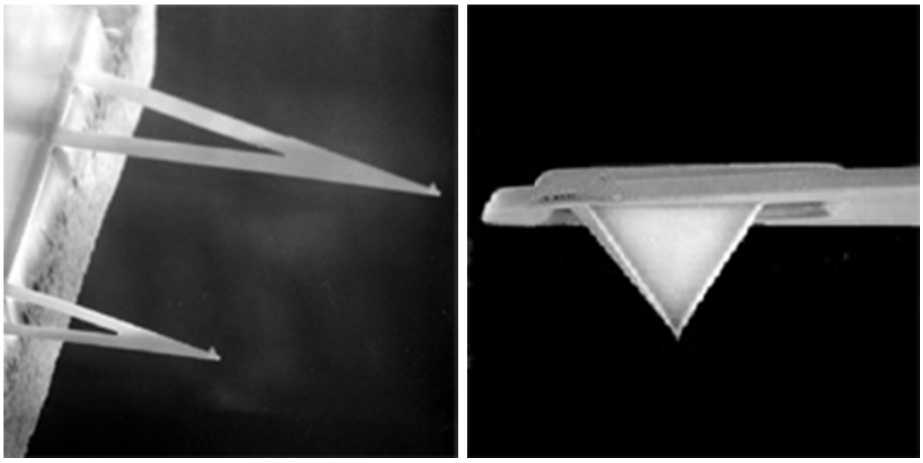

Figure 2-2 Photos of a general purpose silicon nitride cantilever produced by Veeco Probes. Two cantilevers with the tips pointing upwards are shown on the left. A tip is shown on the right. The tip height is 2.5-3.5 μm, the thickness of the cantilever is 0.4-0.7 μm. The triangular cantilever lengths are 196 μm and 115 μm respectively.

<URL: https://www.veecoprobes.com/probe_detail.asp?ClassID=17> [Accessed 22 Feb 2008]

2.1.1.2 Operation Modes of AFM

The AFM is available in several operating modes, including contact mode and tapping mode, which are chosen depending on the sample, environment, and measurements required.

In contact mode (CM), the AFM cantilever is deflected by the sample surface (Yang *et al.*, 2003). Generally, the cantilever deflection is kept constant by the use of a piezoelectric feedback system which permanently regulates the vertical (z) position of either the tip or the sample and produces a constant force image (Bonnell 2001). The image represents the topographic structure of the surface. Deflection is not the most sensitive measurement, having a relatively small signal-to-noise ratio. Furthermore, due to direct contact with the sample, the scanning motion induces lateral forces onto the material which can be intolerable for soft surfaces. However, in some cases, contact mode is still the imaging mode of choice. For example, the alternative modes do not provide the direct information of the force applied onto the sample surface by the tip (Salvetat 1999).

Tapping mode (TM) uses an alternative and more sensitive measurement: the vibrational characteristics of the cantilever. The mechanical resonant frequency of the cantilever is determined by the dimensions of the structure and the properties of materials from which it is made. The vibration amplitude detected at a given frequency changes as a function of the force gradient. Varying the vertical position of the tip such that the amplitude of oscillation at a particular frequency is constant produces a constant force gradient image. TM has a larger signal-to-noise ratio than does CM (Bonnell 2001). It also generates smaller lateral forces on the sample, which improves the lateral resolution of the AFM image, as well as

reducing the damage to the sample while scanning. Consequently, TM is often preferred over CM for most biological applications (Yang *et al.*, 2003).

Phase imaging is relatively new and has the advantage of being able to be performed at the same time as topographic imaging with tapping mode, i.e. both topographic and phase images can be obtained in a single scan. Because the interactions between the tip and the surface depend not only on the topography of the sample but also on other characteristics (such as hardness, elasticity, adhesion, or friction), the movements of the cantilever to which the tip is attached depend also on these properties. In phase imaging, the phase of the sinusoidal oscillation of the cantilever is measured relative to the driving signal applied to the cantilever to cause the oscillation. Phase images are produced by recording this phase shift during the tapping mode scan. Phase imaging can detect, for example, different components in polymers related to their stiffness or areas of different hydrophobicity in hydrogels immersed in saline solutions (Magonov and Reneker 1997).

2.1.1.3 Force Measurements by AFM

In addition to imaging AFM can also probe elastic properties or adhesion on a surface by generating force curves. These curves are generated by performing controlled vertical tip-sample interactions, without lateral scanning movement and while recording the cantilever's deflections. Force curves measure nano- to pico-Newton range vertical forces applied to the surface, and allow the estimation of the nanomechanical properties of the samples. The ability to coat the tip with different molecules (proteins, lipids) has increased the utility of force curves in understanding the specific attraction between a ligand and its receptor (Dammer *et*

al. 1996; Vinckier *et al.* 1998). This technique can also be used to measure charge densities on surfaces (Heinz and Hoh 1999), to estimate the folding force of biomolecules like titin (Rief *et al.* 1997), and to measure forces associated with polymer elongation (Rief *et al.* 1998).

Conversion of force curves

The direct result of a force measurement is a curve of the photodiode current I versus height position of the piezoelectric translator Z_P. In order to obtain the curve of tip-sample interactive force F versus piezo displacement Z_P, the I signal must be converted to F. This is explained as follows by an ideal example as in **Figure 2-3**, which is a model curve as would be observed for an infinitely hard sample surfaces with no surface forces. The curves of the tip approaching to and retracting from the surface are identical. The horizontal part (**Figure 2-3** A-B) is the non-contact line. The linearly increasing part (**Figure 2-3** B-C) is the contact line, from the slope of which the sensitivity $\Delta I/\Delta Z_P$ can be obtained. The I signal can be converted into a cantilever deflection Z_c by dividing the I signal by the sensitivity, which leads to $Z_c = I/(\Delta I/\Delta Z_P)$. Knowing the spring constant of the cantilever k_c, the I signal can easily be converted into force according to Hooke's Law: $F = k_c Z_c$. The non-contact line defines zero deflection of the cantilever, which is therefore the zero force line (Butt *et al.* 2005).

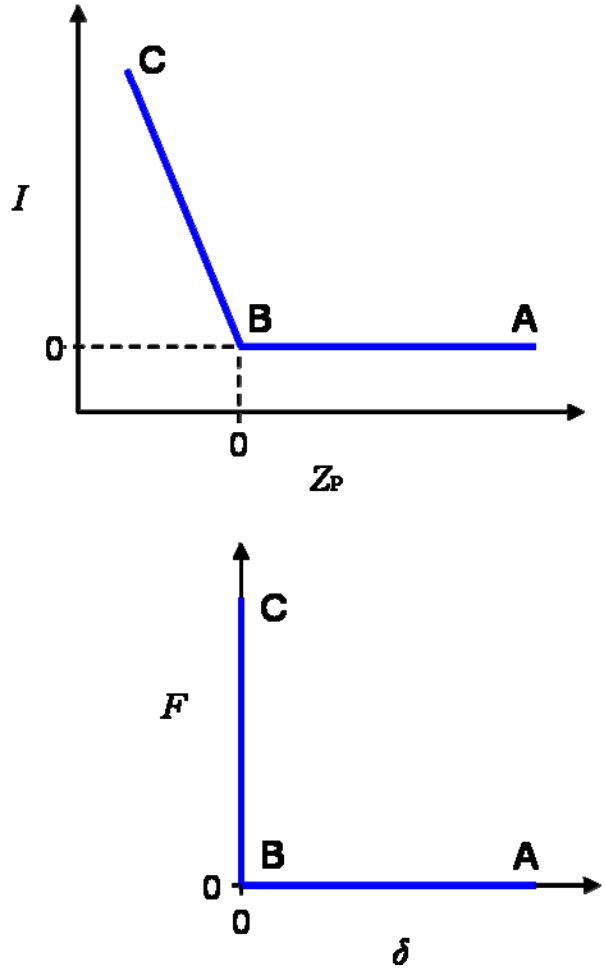

Figure 2-3 A model force measurement curve recorded for an infinitely hard material surface with no surface forces. The approaching and retracting curves are identical. The I vs. Z_P curve is converted to F vs. δ curve. A-B is the non-contact line and B-C is the contact line.

Problem of zero tip-sample distance

The true tip-sample distance, or the indentation δ is the piezo displacement Z_P deduced by the cantilever deflection Z_c: $\delta = Z_P - Z_c$. Using the ideal example of an infinitely hard sample surface without surface forces again (**Figure 2-3**), the definition of zero indentation is as follows: The zero cantilever deflection Z_{c0} lies on the horizontal non-contact line (**Figure 2-3** A-B). The point where the two linear

parts of the force curve cross is defined as zero piezo displacement Z_{P0} (**Figure 2-3** B). The curve of force F versus piezo displacement Z_P then can be converted to force F versus indentation δ (= (Z_P - Z_{P0}) - (Z_c - Z_{c0})) curve.

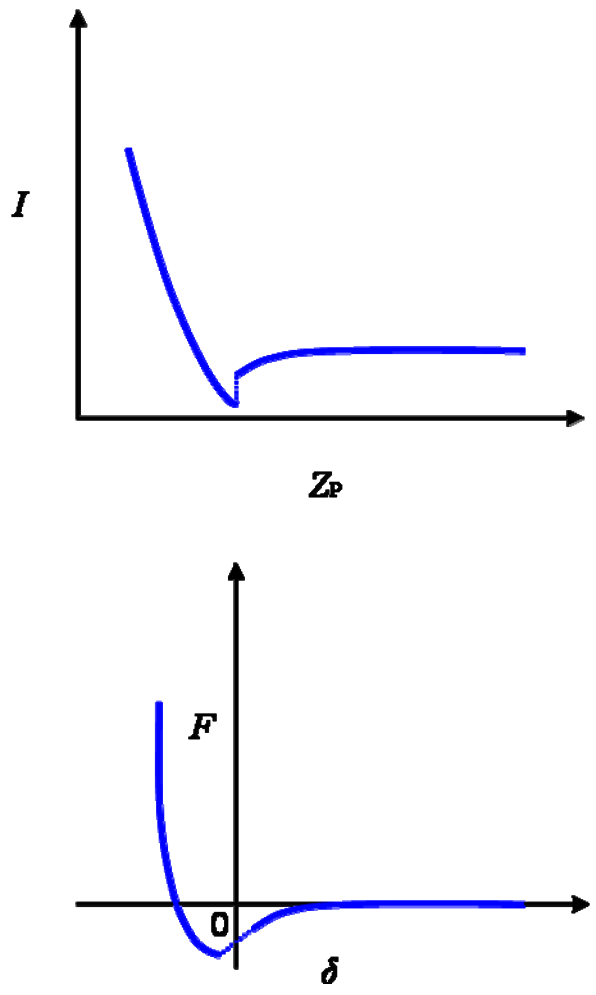

Figure 2-4 A force measurement retracting curve for a deformable material with attraction and adhesion forces. The I vs. Z_P curve is converted to F vs. δ curve.

However, in reality, especially for biological samples, the definition of zero indentation is more complicated. A typical retracting force curve of deformable materials with surface forces is displayed in **Figure 2-4**. Note that for deformable materials, the approach and retract curves of a force measurement are no longer

identical. The approach curve is used to define zero tip-sample distance. The zero cantilever deflection lies on the horizontal non-contact line at large distances away from the surface, where surface forces are negligible. The sensitivity is obtained from the linear contact part of the approach curve. One way to find the zero piezo displacement Z_{P0} is to extrapolate the two linear regimes of the approach curve. Another way to find Z_{P0}, which is more robust and reliable, is to fit experimental data in the range on the approach curve when the tip and sample are in contact using a Hertzian model as described in **Equation 2-1** (Hertz 1882; Rotsch *et al.* 1999; Bhanu and Hörber 2002).

$$Z_P - Z_{P0} = (Z_c - Z_{c0}) + \sqrt{\frac{k_c \cdot (Z_c - Z_{c0})(1-\upsilon^2)}{(2/\pi)\cdot E \cdot \tan(\alpha)}}$$

Equation 2-1

where k_c is the spring constant; α is the half-opening angle of a conical shaped tip; v is the Poisson ratio and E is the elastic modulus. E and Z_{P0} are two unknown variables, which are determined by the fit. By employing a Monte Carlo fit, it is possible to optimize values of E and Z_{P0}. Igor software (Igor Pro version 4; WaveMetrics, OR, USA) was used to perform this type of fitting in chapter **5** of this thesis.

Determination of spring constant of the cantilever

For AFM force measurements, the value of spring constant of the cantilever is usually needed. Several methods have been described, but many do not appear to be simple, reliable and precise at the same time (Albrecht *et al.* 1990; Butt *et al.* 1993; Neumeister and Ducker 1994; Sader 1995; Sader *et al.* 1995, 1999; Senden and Ducker 1994; Cleveland *et al.* 1993; Gibson *et al.* 1996).

Hutter and Bechhofer (1993) proposed an elegant and widely used method, which is implemented in many commercial AFMs. They suggested to measure the intensity of the thermally excited cantilever oscillations or the cantilever thermal noise. For an ideal spring of spring constant k_c, the mean square deflection of the cantilever is:

$$\left\langle Z_c^2 \right\rangle = \frac{k_B T}{k_c}$$

Equation 2-2

where k_B is the Boltzmann constant and T is the absolute temperature.

In reality, considering the shape of the cantilever (which leads to several possible vibration modes) (Butt and Jaschke 1995) and the systematic error of the deflection detecting technique (usually optical lever technique) (Stark *et al.* 2001), there is:

$$k_c = \beta^* \frac{k_B T}{\left\langle Z^{*2} \right\rangle}$$

Equation 2-3

where Z^* is the effective deflection, which is the deflection read from the instrument after determining the sensitivity from the contact part of a force curve on a hard substrate; β^* is the effective correction factor, which is 0.817 for a rectangular cantilever and 0.764 for a V-shape cantilever (Stark *et al.* 2001).

In practice, a force curve is acquired on a hard substrate to characterize the sensitivity, and then a noise spectrum of the deflection amplitude is taken. This spectrum shows a peak at the resonance frequency. The peak is fitted with a Lorentzian curve and the mean square deflection of the peak is obtained by

integration. The thermal noise method was used to obtain the spring constant of cantilever in chapters **5** and **6** of this thesis.

2.1.2 AFM Analysis

AFM Imaging

AFM imaging experiments presented in section **3.1**, **3.2**, **4.2**, **4.3** and **6.2** were carried out using MultiMode scanning probe microscope with Nanoscope IIIa controller (Veeco, Metrology Group, Santa Barbara, CA, USA) equipped with an E-scanner (maximum scan size 10 μm × 10 μm, vertical range 2.5 μm). AFM imaging experiments presented in section **3.3**, **4.4** and **6.3.1** were carried out using the same MultiMode AFM equipped with a J-scanner (maximum scan size 125 μm × 125 μm, vertical range 5.0 μm).

For the AFM imaging experiments presented in section **6.3.2** and **6.3.3**, an EnviroScope AFM (eScope AFM; Digital Instruments) was used. This AFM has an enclosed sample chamber allowing the control of temperature (from room temperature up to 185ºC in air) and humidity (range of 0-80% RH).

Silicon probes (OMCL-AC160TS, Olympus Optical, Tokyo, Japan) with nominal spring constant 34.4~74.2 N/m were used for images obtained using tapping mode in air. V-shaped silicon nitride levers (Veeco Probes, Camarillo, CA, USA) with a nominal spring constant of 0.32 N/m were used for images obtained using tapping mode in liquid. The V-shaped silicon nitride levers (Veeco Probes) with nominal spring constants of 0.06 N/m were used for contact mode in air (these are all manufacturer's data). Scan rates employed were typically 1.0-2.0 Hz.

AFM force measurements

Force measurements presented in chapter **5** were carried out using MultiMode AFM equipped with a Picoforce module (Digital Instruments). V-shaped silicon nitride levers (Veeco Metrology Group) with nominal spring constants of 0.06 N/m (manufacturer's data) were used for force measurements.

2.1.3 Image Processing

AFM image data were analyzed with SPIP software (The Scanning Probe Image Processor, Version 3.3.9.0; Image Metrology A/S, Denmark). It should be noted that, in this thesis, the "height" of a sample means the vertical difference between the top of the sample and the substrate surface; while the "width at the half height" means the horizontal width of a sample at the half of the height of the sample. It is demonstrated in **Figure 2-5** how the height and the half height width of a diphenylamine nanotube from an AFM height image were determined using SPIP software.

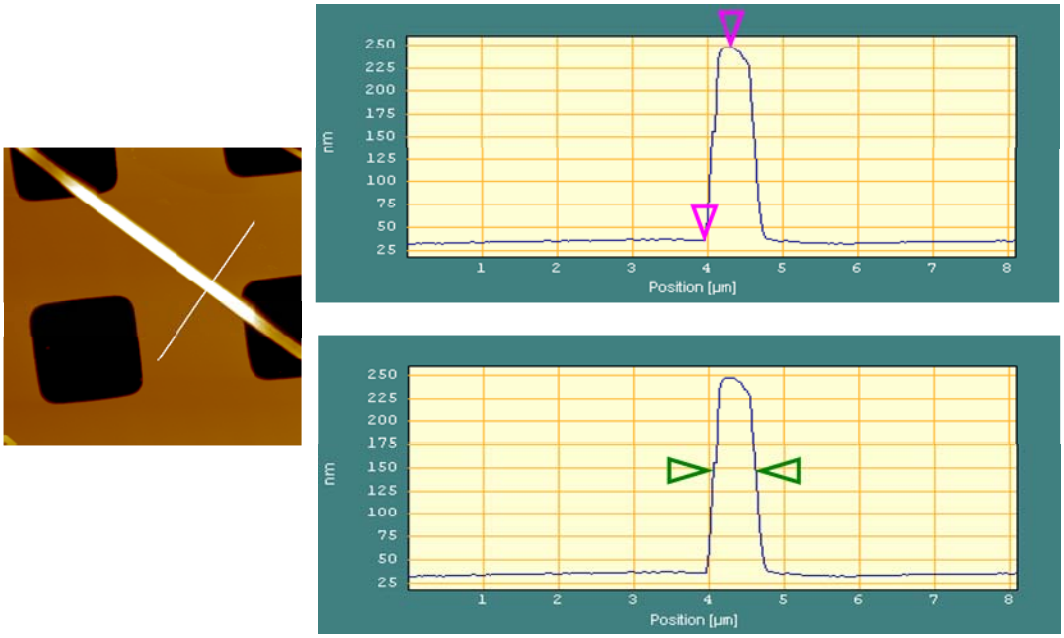

Figure 2-5 Measurement of the dimensions of a protein nanotube from an AFM height image using SPIP. The left picture is an AFM height image of a diphenylalanine nanotube on silicon grid substrate with square holes of 5 µm × 5 µm. The two pictures on the right are the profiles along the white line (which is perpendicular to the direction of the nanotube of interest) on the left image. The vertical difference between the tips of the two pink triangles on the top right profile is the "height" of the nanotube. The horizontal difference between the tips of the two green triangles on the bottom right profile is the "width at the half height".

2.2 Preparation of Protein Nanotubes

2.2.1 Bacterial Flagellar Filaments

Salmonella flagellar filaments were removed from cells by mechanical shearing. Deflagellated cells were removed by centrifugation, and then the flagellar filaments were collected by ultracentrifugation. *Salmonella* flagellar filament samples were stored in 10mM HEPES (pH 7.0, pKa 7.31) and were kindly

provided by Dr. Richard Woods from Queen's Medical Centre (QMC), University of Nottingham.

2.2.2 Lysozyme Fibrils

Chicken egg-white lysozyme (dialyzed lyophilized powder; Sigma Chemical Company, St. Louis, MO, USA) was dissolved to 10mg/mL in 10mM glycine ($C_2H_5NO_2$; SigmaUltra; Sigma Chemical Company) buffer (pH 2.0). Then lysozyme solution was incubated in an electrical oven at 57 ± 2 °C (Krebs, *et al.* 2000).

2.2.3 β2-Microglobulin Fibrils

β2-microglobulin (lyophilized powder; Sigma) was dissolved to 2mg/mL in 25mM sodium acetate (CH_3COONa; Sigma) and 25mM sodium phosphate (Na_3PO_4; Sigma) buffer (pH2.5). Then β2-microglobulin solution was incubated at 37 °C in an incubator.

2.2.4 Diphenylalanine Nanotubes (FF Nanotubes)

The diphenylalanine peptides were purchased from Sigma-Aldrich (Gillingham, Dorset, UK). Fresh stock solutions were prepared by dissolving the lyophilised peptides in 1,1,1,3,3,3-hexafluoro-1-propan-2-ol (HFIP) (Sigma Aldrich) at a concentration of 100 mg/mL. In a typical preparation, a stock solution of ~20 μL was made in an eppendorf tube.

The diphenylalanine peptides stock solution was diluted in double distilled H_2O to a final concentration of 2 mg/mL. In a typical preparation, 2 μL peptides stock solution was added into 98 μL distilled H_2O in an eppendorf, and the sample solution was vortexed for 20~30 seconds. An aliquot of 10 μL of sample solutions

were then immediately dropped onto the substrates and were subsequently dried under a gentle flow of nitrogen.

2.2.5 Sample Preparation for AFM Analysis

Substrates employed for AFM analysis

The substrates used in this thesis were mica, gold or silicon grid.

Mica (Agar Scientific, Essex, UK) surfaces were freshly cleaved prior to sample application.

Gold substrates were prepared by coating gold onto freshly cleaved mica surfaces using an evaporation gold coater. Gold was deposited at ~280 °C under 10^{-6} mbar, and then annealed at ~320 °C for 24 hours (Hegner *et al.* 1993; Wagner *et al.* 1995; Huang *et al.* 2001). The gold substrate was then UV cleaned (UV cleaner from Scientific & Medical Products Ltd., Cheshire, UK) for 10 minutes prior to applying the nanotube sample. Gold substrate prepared in this way had flat islands (typically 0.2 μm to 1.0 μm in width), separated by gaps ~30 nm to ~150 nm in width (**Figure 2-6**).

Micropatterned silicon substrates (with holes of 5 μm × 5 μm and 200 nm deep) (**Figure 2-7**) were cleaned with the UV cleaner (Scientific & Medical Products Ltd.) for 10 minutes prior to applying the sample.

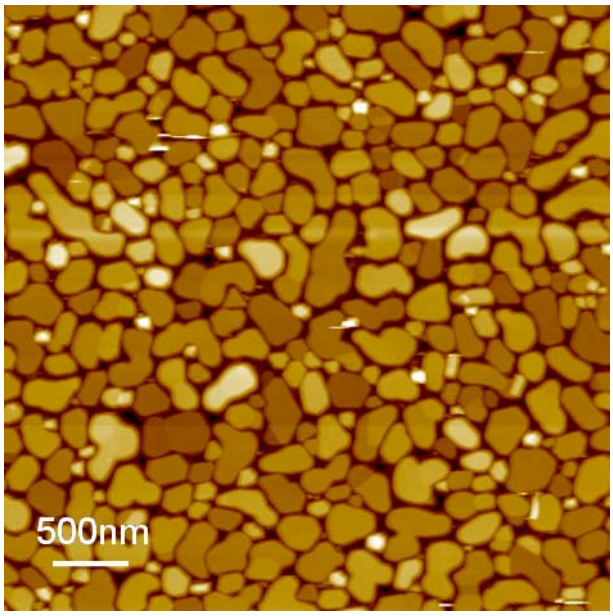

Figure 2-6 AFM height image of gold substrate obtained using evaporation gold coater. The image was obtained in tapping mode in water. There are gaps between gold plateau. Those gaps are ~30 nm to ~150 nm in width. The Z-range of the image was 237.3 nm.

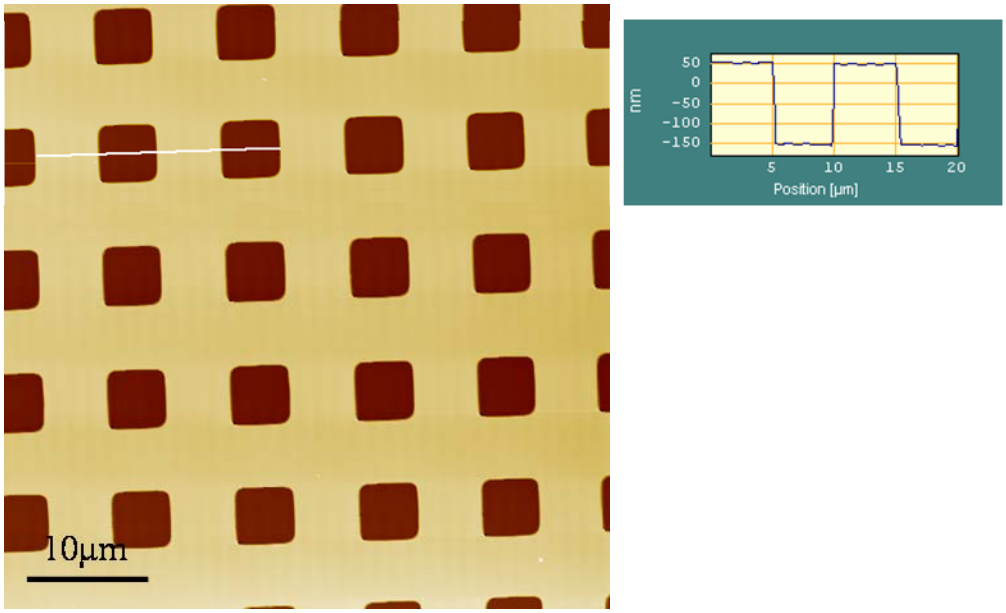

Figure 2-7 An AFM height image of a micropatterned silicon substrate with holes of 5 µm × 5 µm and 200 nm in depth. The pitch of this substrate is 10 µm. The right picture is the profile of the white line on the left image, which shows two pitches of the substrate.

General sample preparation protocols for AFM analysis

The general protocol for sample preparation for AFM analysis was as follows:

Stocks of samples were first diluted with a range of solutions employed for AFM sample preparation. These solutions were prepared from the following chemicals as needed: Hydrochloride acid (36.5-38.0%), sodium hydroxide (pellet), propanol (anhydrous), phosphate-buffered saline (tablet), magnesium chloride (power), which were also purchased from SIGMA®.

For AFM imaging in air, a 10 μL droplet of the appropriate sample solution was applied to a substrate. The sample solution was left to stand on the substrate for a certain time to allow the sample to deposit onto the mica surface; samples were then rinsed using distilled water, and then dried in a gentle flow of nitrogen. Rinsing the surface was required to remove solution components, but care was taken as over-washing could denature samples and also decrease the coverage. Under-drying can potentially reduce AFM resolution because samples can move around on moist surfaces. Conversely, over-drying can alter the features of the samples because of dehydration of the protein (Bonnell 2001). The mica with the sample was attached to a metal stub using double-sided sticky tape and mounted onto a strong magnet located on the sample stage.

For AFM imaging in liquid, a 10μL droplet of the appropriate sample solution was applied to the substrate. The substrate with the sample was attached to a metal stub using double-sided sticky tape and mounted onto a strong magnet located on the sample stage. A standard fluid imaging cell (Veeco) was needed to seal the solution, to prevent evaporation and allow for solution exchange. Solution was injected into the fluid cell with a syringe, and for some experiments, the

solution in the cell had to be changed during experiments. During this latter process new solution was carefully injected into the cell, while old solution was drawn out through the other channel of the cell by a second syringe.

Variation in deposition procedures (for imaging in air or in liquid) can affect the quality of the image. For example, longer deposition times can increase coverage of samples but also increase the chances that the features of the samples are altered by interaction with the surface (imaging in air or in liquid) or by the effects of buffer solution (imaging in liquid). For these studies, the shortest deposition time that provided reasonable surface coverage was optimal.

Chapter 3 Dynamic Processes of Assembly and Degradation of Protein Nanotubes

The AFM is capable of monitoring a range of dynamic processes, including biomaterial assembly and degradation under near-physiological conditions (Engel and Müller, 2000). If the process of interest occurs on the scale of a few minutes to a few hours, and the conditions of such process are suitable for AFM operation, real-time monitoring can be obtained. Otherwise the process needs to be interrupted, and individual samples at certain time parts prepared for AFM analysis. Here three processes occurring on different time scales will be investigated and discussed, as examples to explore this ability of AFM to understand the dynamic properties of protein nanotubes. This chapter also provide the imaging study as foundation to support further studies on physical properties in later chapters (chapter **4**, **5** and **6**).

3.1 Flagellar Filaments in Different Environment

3.1.1 Flagellar Filaments on Mica in Air

Salmonella flagellar filaments were firstly imaged on mica in air, as it is generally the simplest AFM imaging condition (see section **2.2.5**), which establishes the basic experimental conditions for further investigations.

Stock solutions of *Salmonella* flagellar filaments were diluted 100 times using pH 7.0 buffer solution (10 mM PBS), and then imaged using tapping mode AFM in air on mica (**Figure 3-1**; detailed sample preparation see section **2.2**).

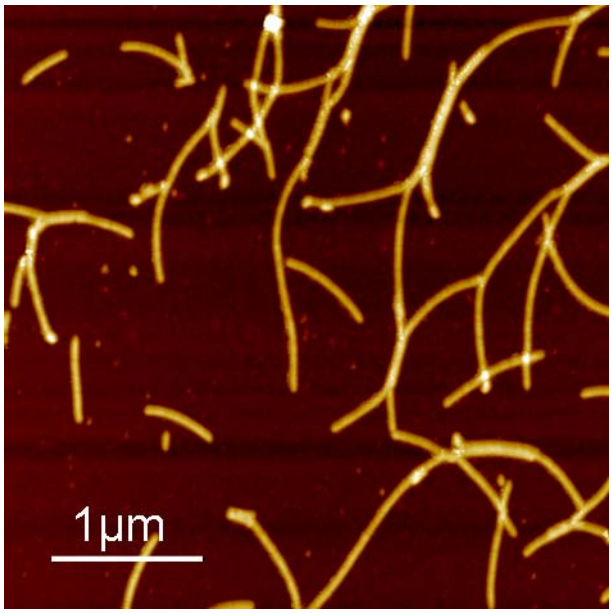

Figure 3-1 Tapping mode AFM height images of *Salmonella* flagellar filaments in air on mica. Stock sample solutions were 100 times diluted. The Z-range is 37.3 nm.

The contour length of *Salmonella* flagellar filaments was found to be 1.0 ± 0.4 μm (**Figure 3-2**). The shorter filaments are most likely the fragments resulted from the mechanical shearing during the filaments preparation (see section **2.2.1**). The average height of the filaments was 4.5 ± 0.6 nm.

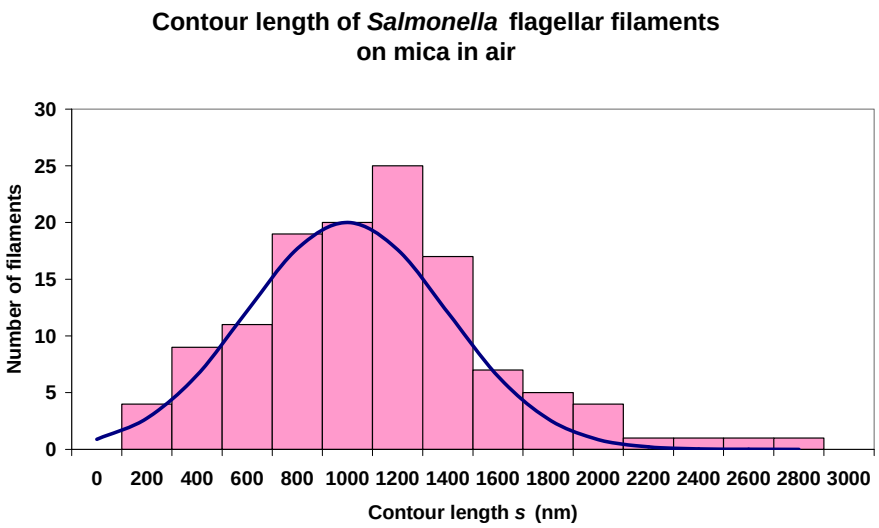

Figure 3-2 Histogram of the contour length measured for *Salmonella* flagellar filaments on mica in air. The mean contour length measured was 1.0 ± 0.4 μm (N = 125).

3.1.2 Dissociation of Flagellar Filaments in Low pH Environment

Salmonella flagellar filaments are known to dissociate in acid environments (Namba and Vonderviszt 1997). Here, in order to directly monitor this dissociation process, the conditions required to image the filaments in aqueous environments first needed to be established.

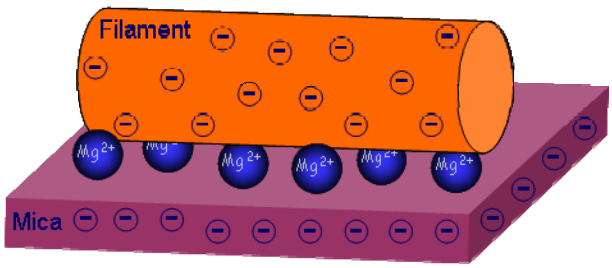

Figure 3-3 A sketch demonstrates that Mg^{2+} works as a bridge between flagellar filaments and the mica surface in pH 7.0 buffer solution.

Because the isoelectric point (p*I*) of flagellin is 5.2 and the amino acid residues on the outer surface of *Salmonella* flagellar filaments are mostly charged residues (Namba and Vonderviszt 1997), in pH > 5.2 solution, the surface of *Salmonella* flagellar filaments will be negatively charged; as is the surface of the mica substrate (Vesenka *et al.* 1992). Therefore, without the inclusion of additional ions, the imaging of the *Salmonella* flagellar filaments on mica substrates is problematic due to poor immobilization. Two methods were explored to resolve this problem. First, magnesium ions (Mg^{2+}) were added into solution to immobilize the *Salmonella* flagellar filaments onto the mica surface (**Figure 3-3**) (Vesenka *et al.* 1992, see section **3.1.1** and **3.1.3**); second, AFM images were obtained at a pH at least lower than 5.2 (see section **3.1.2**).

3.1.2.1 Salmonella Flagellar Filaments in Neutral Condition

Salmonella flagellar filaments were first imaged in pH 7.0 solution. A height image taken in pH 7.0 buffer solution (10 mM PBS & 10 mM $MgCl_2$) using tapping mode AFM is displayed on **Figure 3-4**. To prepare samples for imaging, stock solution of *Salmonella* flagellar filaments (for preparation of stock solution see section **2.2.1**) was diluted 100 fold using pH 7.0 buffer solution (10 mM PBS & 10 mM $MgCl_2$). A 10 μL droplet of diluted sample solution was spread on a freshly cleaved mica surface, and left for 1hour on mica, before covering with pH 7.0 buffer solution (10 mM PBS & 10 mM $MgCl_2$) for AFM imaging. There are two long filaments and two short filaments visible in **Figure 3-4**. Some very short flagellar filament fragments can also been seen in **Figure 3-4**, which were probably produced during the mechanical shearing process when the flagellar filaments were removed from the living cells (see section **2.2.1**).

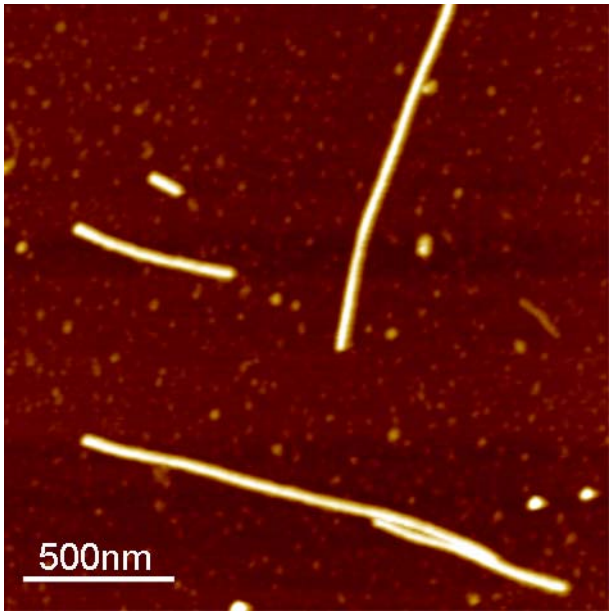

Figure 3-4 A height image of *Salmonella* flagellar filaments taken in pH 7.0 buffer solution (10 mM PBS & 10 mM $MgCl_2$) using tapping mode AFM. The Z-range is 9.3 nm.

3.1.2.2 Salmonella Flagellar Filaments in Weak Acidic Condition

As stated above, in low pH solution (pH<5.2), *Salmonella* flagellar filaments would be positively charged, therefore, they could be immobilized directly onto the mica surface via electrostatic attraction. A height image taken in pH 4.4 solution using tapping mode AFM is displayed in **Figure 3-5**. Stock solution of *Salmonella* flagellar filaments was diluted 100 fold by HCl to achieve a final pH of 4.4 for AFM imaging. A 10 μL droplet of sample solution was spread on a freshly cleaved mica surface and left for 1.5 h before covering with HCl (pH 4.4) solution for AFM imaging.

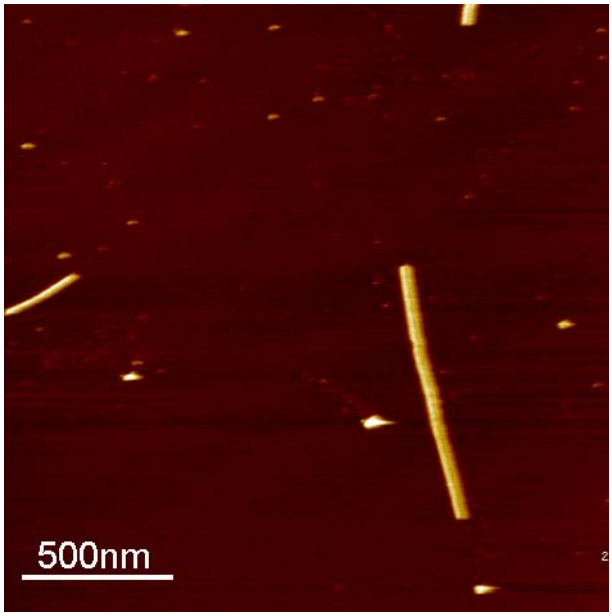

Figure 3-5 A height image of *Salmonella* flagellar filaments taken in HCl solution (pH 4.4) using tapping mode AFM. The Z-range is 14.2 nm.

3.1.2.3 Salmonella Flagellar Filaments in Alkaline Condition

Salmonella flagellar filaments were also imaged in alkaline solution, with the presence of Mg^{2+} ions. A height image taken in pH 10.0 solution (0.1mM NaOH & 10 mM $MgCl_2$) using tapping mode AFM is displayed on **Figure 3-6**. The stock solution of *Salmonella* flagellar filaments was diluted 100 fold with solution (0.1mM NaOH & 10 mM $MgCl_2$) to a final pH of 10.0 for AFM imaging. A 10 μL droplet of sample solution was spread on a freshly cleaved mica surface and allowed to stand for 1h before covering with solution (0.1mM NaOH & 10 mM $MgCl_2$, pH 10.0) for AFM imaging.

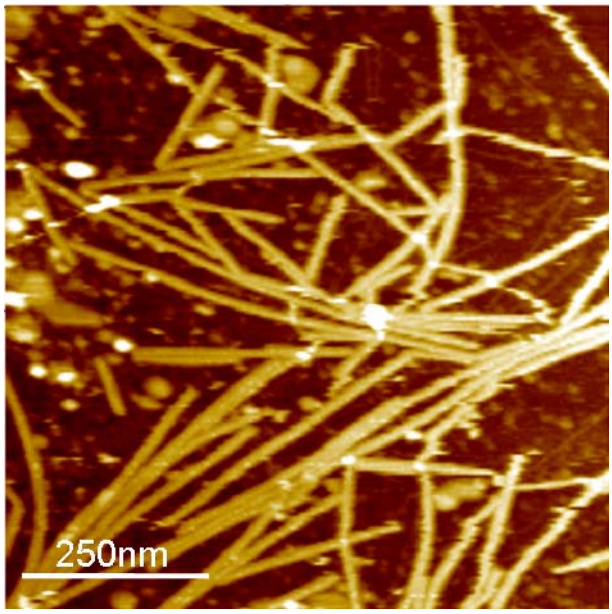

Figure 3-6 A height image of *Salmonella* flagellar filaments taken in pH 10.0 solution (0.1mM NaOH & 10 mM $MgCl_2$) using tapping mode of AFM. The Z-range is 22.6 nm.

The results of AFM experiments of *Salmonella* flagellar filaments in acidic, alkaline and neutral environments are presented in **Table 3-1** for comparison. The dimensions were measured using SPIP software (see section **2.1.3**).

The cross section of *Salmonella* flagellar filaments is known to be circular (Mimori *et al*. 1995; Morgan *et al*. 1995). However, measured from AFM images, the diameters were found to be bigger than the height measurements (**Table 3-1**). This may because of three reasons: First, it may be due to tip broadening phenomena. Tip broadening arises when the radius of curvature of the tip is comparable with, or greater than, the size of the feature being imaged (West and Starostina n.d.). The diagram in **Figure 3-7** illustrates this problem. As the tip scans over the filament, the sides of the tip make contact before the apex, and the microscope begins to respond to the feature. Second, the pressure caused by the AFM tip may also result in compression of the *Salmonella* flagellar filaments

(Morris *et al.* 1999). Third, the attraction between the *Salmonella* flagellar filaments and the mica surface may also result in some compression and a decrease the height of the filaments (Israelachvili 1992).

Table 3-1 The dimensions of *Salmonella* flagellar filaments observed in AFM images obtained in liquid.

pH of the solutions	pH 4.4	pH 7.0	pH 10.0
Diameter D (nm)	33.7 ± 0.8	26.8 ± 0.8	34.2 ± 0.9
Height H (nm)	7.2 ± 0.6	9.1 ± 0.5	7.1 ± 0.6
Length L (μm)	1.0 - 3.0		
N	5	8	10

N is the number of *Salmonella* flagellar filaments measured; *D* is the average diameter of *Salmonella* flagellar filaments; *H* is the average height of *Salmonella* flagellar filaments; *L* is the length range of the most *Salmonella* flagellar filaments observed. All the images were taken in liquid using tapping mode AFM and analyzed using SPIP software (see section **2.1.3**).

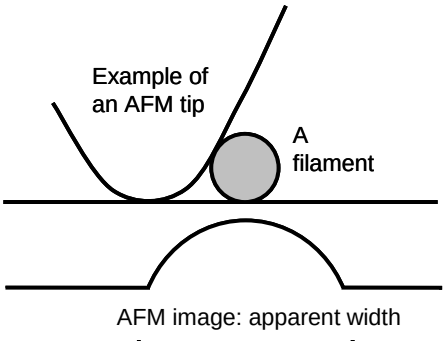

Figure 3-7 Sketch of an example of "tip broadening" effect on a filament. On the bottom a resulting scan line is shown.

Although the dimensions of *Salmonella* flagellar filaments in AFM images may be affected by the difference of the AFM tips and/or the imaging conditions employed (e.g. set point), the observed dimensions may still provide useful information on the environmental effect on the filaments. For example, the average diameter of *Salmonella* flagellar filaments measured in pH 4.4 solution was ~33% wider than in pH 7.0 solution; while the average height measured in pH 7.0 solution was ~24% less in pH 4.4 solution. This may because *Salmonella* flagellar filaments were "softer" and more compressible by AFM tip under low pH environment.

The height and the diameter of the filaments in alkaline solution are close to the dimensions of the filaments in weak acidic solution, which indicates that the conformations of *Salmonella* flagellar filaments in acidic and alkaline environments may be similar (Kamiya and Asakura 1976; also see section **1.2.2.3**).

3.1.2.4 Dissociation of Salmonella Flagellar Filaments in Acidic Condition

Salmonella flagellar filaments are not stable in low pH environments (pH<4.4), where they are likely to be dissociated into single flagellin proteins (Namba and Vonderviszt 1997).

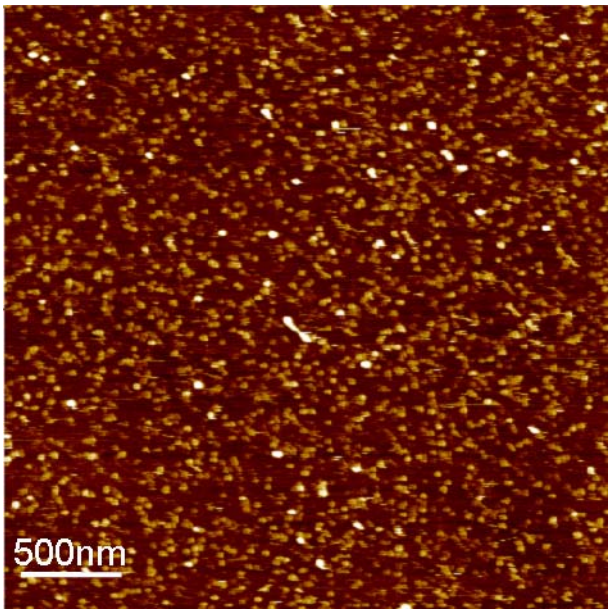

Figure 3-8 A height image of *Salmonella* flagellar filaments taken in pH 4.0 solution using tapping mode of AFM. The Z-range is 8.8 nm.

A height image of *Salmonella* flagellar filaments taken in pH 4.0 solution using tapping mode AFM is displayed in **Figure 3-8**. Sample solution was allowed to stand for 1 h on mica before imaging. The average height of the particles observed in this image is 2.4 ± 0.3 nm. The particles are most likely single flagellin or subunits of several flagellins (Namba and Vonderviszt 1997). From the sample preparation of these images it was clear that *Salmonella* flagellar filaments dissociated in pH 4.0 solution within 1 h. Therefore to directly observe the process of dissociation, the experiment of changing the pH of solution while imaging was performed.

3.1.2.5 Direct Observation of the Dissociation of Salmonella Flagellar Filaments in Acidic Condition

The dissociation of *Salmonella* flagellar filaments in acidic solution is shown in **Figure 3-9**. Three filaments were initially imaged in pH 7.0 PBS solution. Image (a) was taken right after the injection of 1mM HCl into the fluid cell (see section **2.2.5**), no visible dissociation was observed. Image (b) was taken 20 minutes after the injection. Most parts of the three filaments had undergone a dissociation process, though several fragments of filaments could still be seen (e.g. a fragment in the centre of the cross) in image (b). Image (c) was taken 40 minutes after the injection. There were almost no fragments remaining in image (c). Image (d) was taken 1 hour after the injection. The filaments were completely dissociated into particles and diffusing away from the original site.

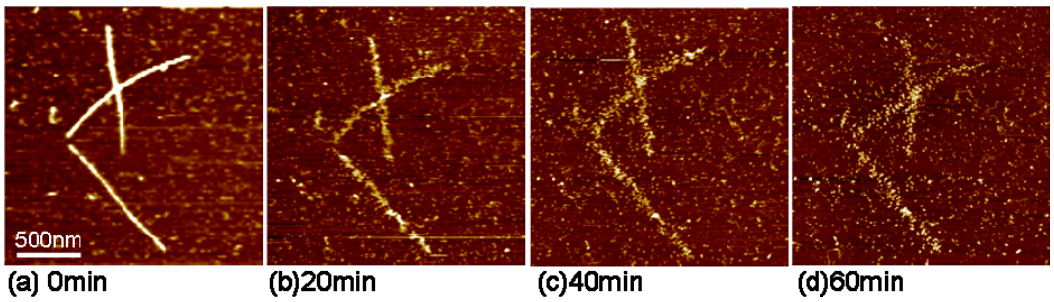

Figure 3-9 Height images of *Salmonella* flagellar filaments in liquid using tapping mode AFM. The sample was in pH 7.0 buffer solution (10 mM PBS & 10 mM $MgCl_2$) at first, then 1mM HCl was injected into the sample solution. (a) was taken right after injection; then (b) was taken 20 min after injection; (c) was taken 40 min after injection; (d) was taken 1 h after injection. The Z-range is 9.9 nm.

This was the first time that the dissociation process of *Salmonella* flagellar filaments in low pH solution has been visualised by AFM. This study provided highly valuable information for the development of applications for *Salmonella* flagellar filaments. Most of the intersubunit interactions found within the outer tube of flagellar filaments are polar–polar or charge–polar (Yonekura *et al.* 2002; 2003; also see section **1.2.2**). When basic residues are protonated, the interactions between flagellin break down. All parts of a filament exposed to the low pH solution were found to break down instantly. The centre piece fragment of the cross in image **Figure 3-9** (b) was probably a fragment from the lower filament of the cross on image (a), which survived in the first 20 minutes because of the protection of the upper filament of the cross from the low pH solution. This could be used advantageously in the controlled digestion of flagellar filaments when flagellar filaments are used as scaffolds to obtain nanowires (Kumara *et al.* 2006; 2007; Woods *et al.* 2007, also see section **1.2.3**).

3.1.3 Flagellar Filaments on Gold Surface

Salmonella flagellar filaments on gold substrate also studied. It is part of the study to explore the imaging capability of AFM in different environment, as well as the foundation for studies on physical properties in later chapters (e.g. chapter **4** and **6**).

3.1.3.1 *Salmonella* Flagellar Filaments imaged in Air on Gold Surfaces

Gold substrates were prepared by coating gold onto freshly cleaved mica surface using evaporation gold coater (see section **2.2.5**). Stock solutions of *Salmonella* flagellar filaments were diluted 100 times using pH 7.0 buffer solution

(10 mM PBS) and then imaged using tapping mode AFM in air on gold (**Figure 3-10**; detailed sample preparation see section **2.2**). The average height of the *Salmonella* flagellar filaments observed on the gold substrates was 4.4 ± 0.6 nm ($N = 20$).

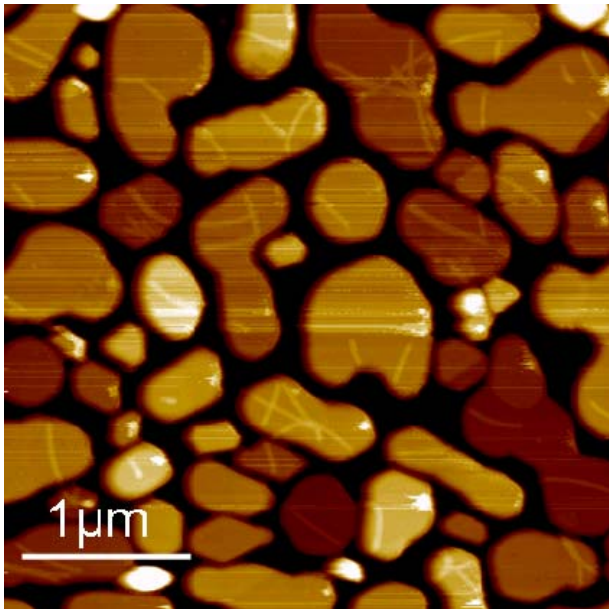

Figure 3-10 Tapping mode AFM height images of *Salmonella* flagellar filaments in air on gold. Stock sample solutions were 100 times diluted. The Z-scale is 351.5 nm.

3.1.3.2 The *Salmonella* Flagellar Filaments in Propanol on Gold Surface

It was found difficult to immobilize *Salmonella* flagellar filaments onto gold substrate while scanning in aqueous buffer solution. However, in propanol or water mixed with propanol (>80% propanol), *Salmonella* flagellar filaments were found to bind to the substrate firmly enough to allow imaging (**Figure 3-11**). This may be due to the dehydration and/or the insolubility of *Salmonella* flagellar filaments in propanol solutions. The dehydration may help to expose the filaments

surface to the probing tip (Hansma *et al.* 1992; 1993; Lyubchenko *et al.* 1993). The influence of imaging condition on the observed filament dimensions was investigated by imaging in a series of propanol-water mixtures **(Table 3-2)** (**Figure 3-12**).

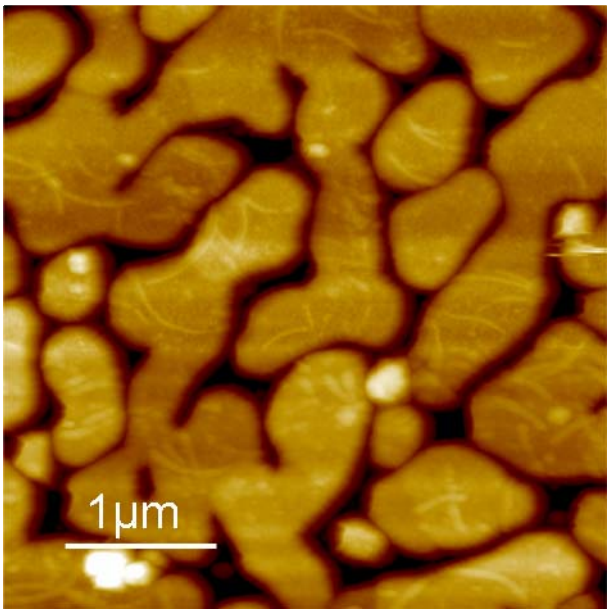

Figure 3-11 Tapping mode AFM height images of *Salmonella* flagellar filaments in 80% propanol on gold. Stock sample solutions were 5 times diluted.

Table 3-2 The average height of *Salmonella* flagellar filaments on gold surface in a series of propanol-water mixtures.

Buffer	100% propanol	90% propanol + 10% water	80% propanol + 20% water
Height (nm)	5.4 ± 0.5	12.2 ± 0.9	17.0 ± 1.1

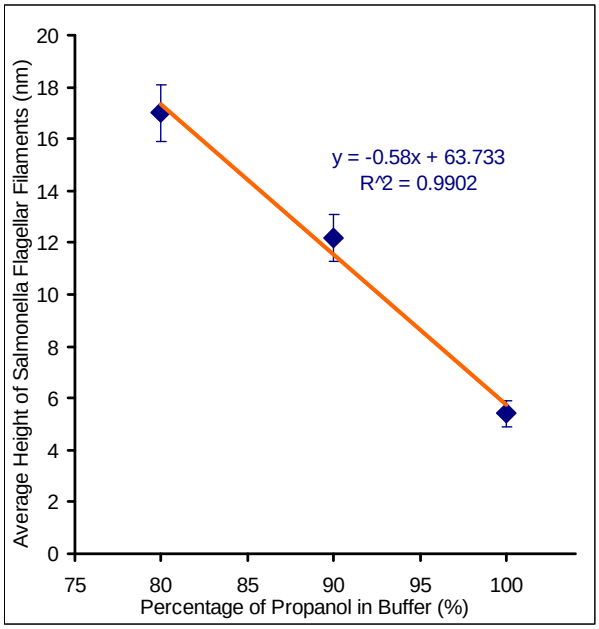

Figure 3-12 A plot of average height of *Salmonella* flagellar filaments vs. percentage of propanol in propanol-water buffer.

In 100% propanol, the average height of *Salmonella* flagellar filaments was close to that observed in air; the average height increased proportionally while the percentage of propanol in buffer decreased. In below a concentration of 70% propanol, *Salmonella* flagellar filaments could not be immobilized onto gold.

3.2 Fibrillization Processes of Lysozyme

Unlike the dissociation of *Salmonella* flagellar filaments in low pH environments which occurred within an hour, the fibrillization of lysozyme takes up to two weeks in laboratory (Krebs, *et al.* 2000, also see section **2.2.2**). Therefore, real-time monitoring of this fibrillization process by AFM imaging is not feasible. In order to observe it, the assembly process has to be interrupted, so that samples can be prepared for AFM analysis.

3.2.1 Preparation of Lysozyme Samples

Lysozyme protein dissolved in glycine buffer was incubated at 57 ± 2 °C (details see section **2.2.2**). After a certain incubation time, the sample was removed from the oven to room temperature and a 10 μL droplet of sample solution spread onto a fleshly cleaved mica surface. After 2 minutes, the mica surface was rinsed with distilled water, and then dried under a gentle flow of nitrogen gas. The sample then was imaged with AFM using tapping mode in air (**Figure 3-16** to **Figure 3-23**). This AFM sample preparation process, especially the drying procedure stopped the continuous fibrillization of lysozyme.

Glycine buffer was imaged under the same conditions before and after incubation as the control experiment (**Figure 3-13**). A few particles (height range from ~2 nm to ~10 nm) were observed on the images, which we attribute to undissolved glycine powder produced when the buffer was prepared.

The initial lysozyme sample was also imaged prior to incubation (**Figure 3-14**). Lysozyme protein is known to have hydrodynamic diameter of 4.1nm (Merrill, *et al.*, 1993). Particles of lysozyme proteins were observed on the AFM images. The average height of lysozyme particles measured from AFM images was 1.6 ± 0.5 nm. A histogram of the height of lysozyme particles was displayed in **Figure 3-15**. The particles observed are most likely single lysozyme proteins or clusters of several lysozyme proteins. The average height obtained however was smaller than the previously known diameter of lysozyme protein. The reduction of the diameter is most likely due to the drying process during the sample preparation and/or the pressure caused by the AFM probe while scanning (Rossell 2003).

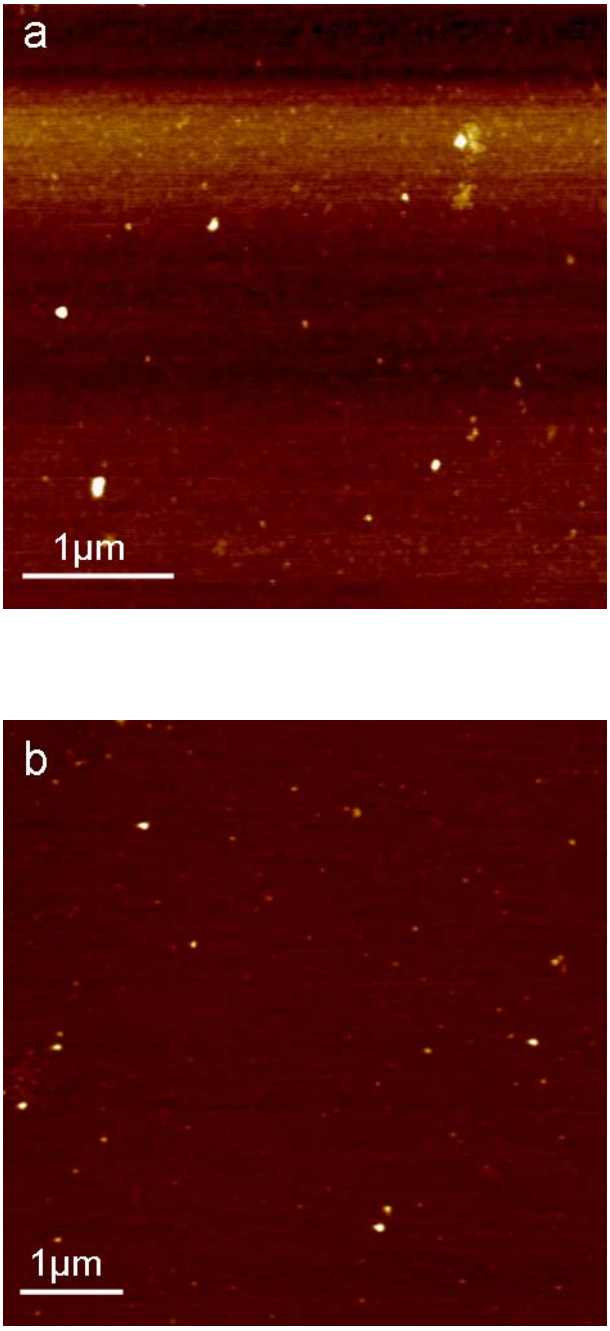

Figure 3-13 An AFM height image of 10 mM glycine buffer obtained using tapping mode AFM before (a) and after (b) incubation at 57 ± 2 °C for 2 weeks. The Z-range is 8.1 nm.

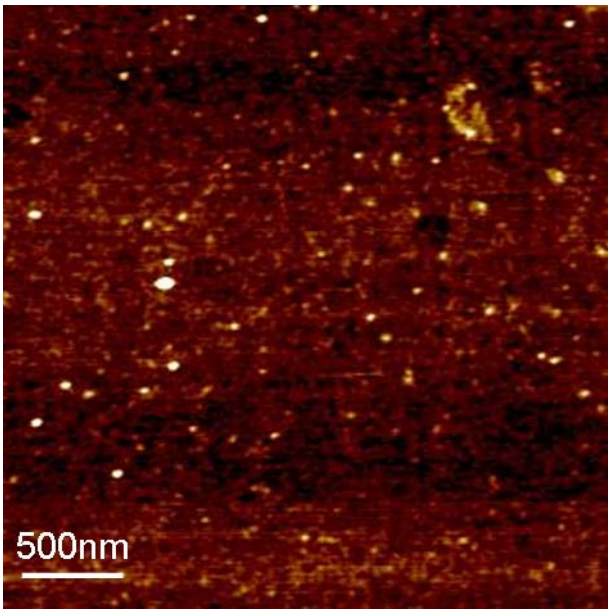

Figure 3-14 An AFM height image in tapping mode of 10mg/mL lysozyme in 10mM glycine buffer at pH 2.0. The Z-range is 9.8 nm.

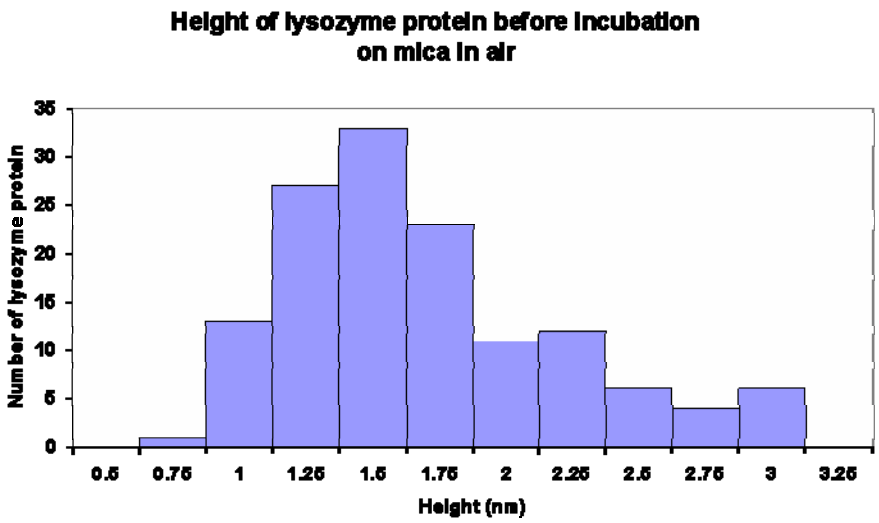

Figure 3-15 Histogram of the height of lysozyme particles before incubation measured from AFM images taken on mica in air. The average height of lysozyme particles was 1.6 ± 0.5 nm (N = 136).

3.2.2 The Early Stages of Lysozyme Fibrillization

Samples from different batches were found to have slightly different rates of fibrillization. Highly flexible protofilaments of elongated lysozyme proteins were however always observed after 2 to 3 days of incubation (**Figure 3-16**).

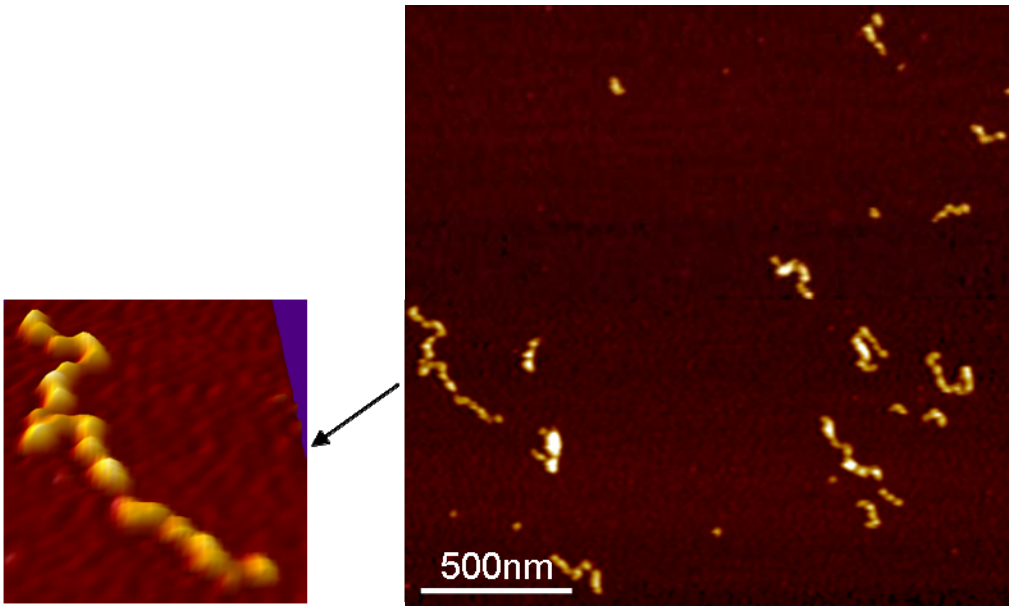

Figure 3-16 An AFM height image of lysozyme after 3 days of incubation. A 3D image (generated by SPIP software) of one protofilament, which is indicated by the black arrow, is displayed on the left. The Z-range is 10.4 nm.

The protofilament appeared to be a chain of single particles (**Figure 3-16**, Jansen *et al.* 2005; Goldsbury *et al.* 2005). The lengths of the protofilaments were from ~80 nm to ~700 nm. The average height of the higher points of the protofilaments was 4.4 ± 0.6 nm; while the average height of the lower points of the protofilaments was 2.9 ± 0.2 nm. Compared to the height of the single lysozyme proteins (1.6 ± 0.5 nm), the elongated particles were (4.4 / 1.6 =) 2.8 times in

height. This suggested that lysozyme proteins had undergone a dramatic structural change in order to form protofilaments (Dobson *et al.*, 1998).

After 2 to 3 days of incubation, along with the protofilaments, a few fibrils with clear periodicities began to be observed. One such fibril is shown in **Figure 3-17**. This fibril has a pitch of 85 ± 4 nm, an average height 5.3 ± 0.9 nm with the average height of the higher points 7.0 ± 0.3 nm and average height of the lower points 3.5 ± 0.1 nm (Jansen *et al.* 2005).

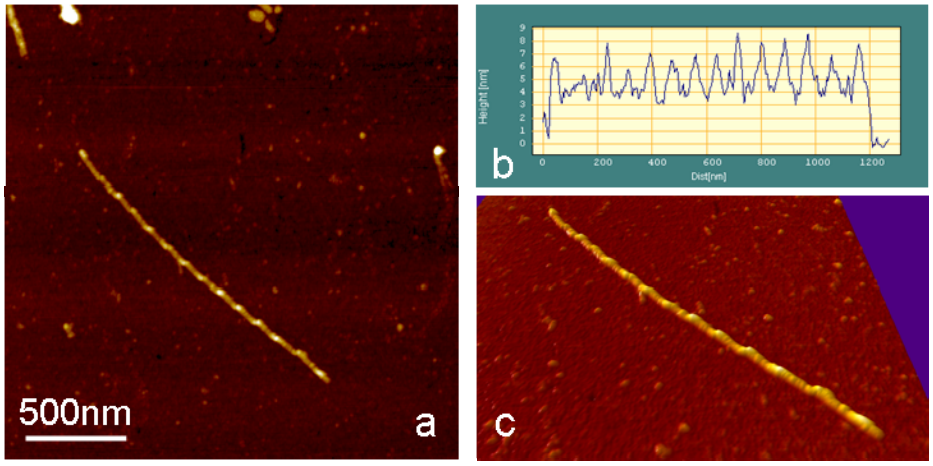

Figure 3-17 AFM image of one lysozyme fibril with clear periodicity after 2 days of incubation; (a) is the height image, (b) is the profile along the axis of the fibril on (a), and (c) is a 3D image of the fibril on (a) generated by SPIP software (see section **2.1.3**). The pitch of this fibril is 85 ± 4 nm. The average height of this fibril is 5.3 ± 0.9 nm with the average height of the higher points 7.0 ± 0.3 nm and average height of the lower points 3.5 ± 0.1 nm. The Z-range is 20.5 nm.

3.2.3 The Middle Stages of Fibrillization

Fibrils with distinct branches splaying apart (**Figure 3-18**, indicated by green arrows) were observed after 4 days of incubation. The highly flexible protofilaments (**Figure 3-18**, indicted by blue arrows) have an average height of 2.3 ± 0.2 nm.

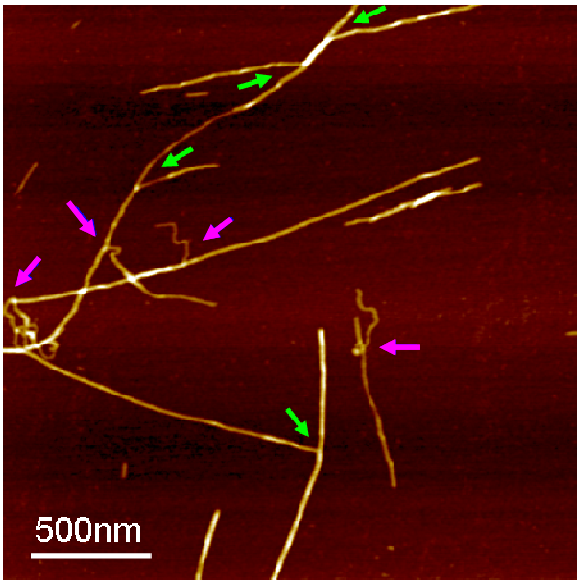

Figure 3-18 AFM height image of lysozyme fibrils after 4 days of incubation. The green arrows indicate fibrils with distinct branches splaying apart. The pink arrows indicate highly flexible protofilaments connected to rigid mature fibrils. The Z-range is 15.9 nm.

Lysozyme fibrils from three different batches on the middle stages of incubation (2 to 10 days) were imaged and categorised according to their heights into 6 types (**Table 3-3**).

As described in section **1.3.1.3**, Khurana and co-workers (2003) proposed a general hierarchical assembly model of amyloid fibrils. For example, the assembly model of insulin into amyloid fibrils is as shown in **Figure 3-19**. Two identical subunits intertwine with each other to form fibrils of a higher assembly

level. The subunit can be a protofilament or a fibril consisting of 2 or 4 protofilaments, and the average height of a fibril is 1.5*D* (*D* is the diameter of the cross section of a subunit), with the height of the higher points 2*D* and the height of the low points *D*.

Table 3-3 The average heights of 6 types of lysozyme fibrils observed. Types II to VI fibrils have clear periodicity. Type I fibrils did not have clear periodicity.

	Type I	Type II	Type III	Type IV	Type V	Type VI
Average height of higher points (nm)	2.3 ± 0.2	4.5 ± 0.3	5.7 ± 0.1	7.0 ± 0.3	7.2 ± 0.2	10.2 ± 0.2
Average height of lower points (nm)		2.5 ± 0.2	3.8 ± 0.1	3.5 ± 0.2	5.4 ± 0.2	6.0 ± 0.1
N	50	30	30	20	9	6

If the assembly of lysozyme fibrils also followed the same model as in **Figure 3-19**, from the height of lysozyme protofilaments (2.3 ± 0.2 nm), the Type I fibrils, the heights of the fibrils would be predicted as shown in **Table 3-4**.

Compared **Table 3-4** with **Table 3-3**, Type II lysozyme fibrils fit well into "1+1" model; Type IV fibrils fit well into "2+2" model; and Type VI fibrils fit well into "4+4" model. However, other types of fibrils do not fit into Khurana's model.

As indicated by pink arrows in **Figure 3-18**, highly flexible protofilaments were observed connected to fibrils of different types. This may therefore suggest a new assembly model i.e. an "n+1" model (where n is the number of protofilaments in one subunit) (**Table 3-5**). In other words, a protofilament might intertwine with a fibril already consisting of more than one protofilament (**Figure 3-20**). The average

height of an "n+1" fibril is $(D_n + D_1)/2$ (D_n is the diameter of the cross section of the subunit consisting of more than one protofilaments; D_1 is the diameter of the cross section of one protofilament), with the height of the higher points $(D_n + D_1)$ and the height of the lower points D_n.

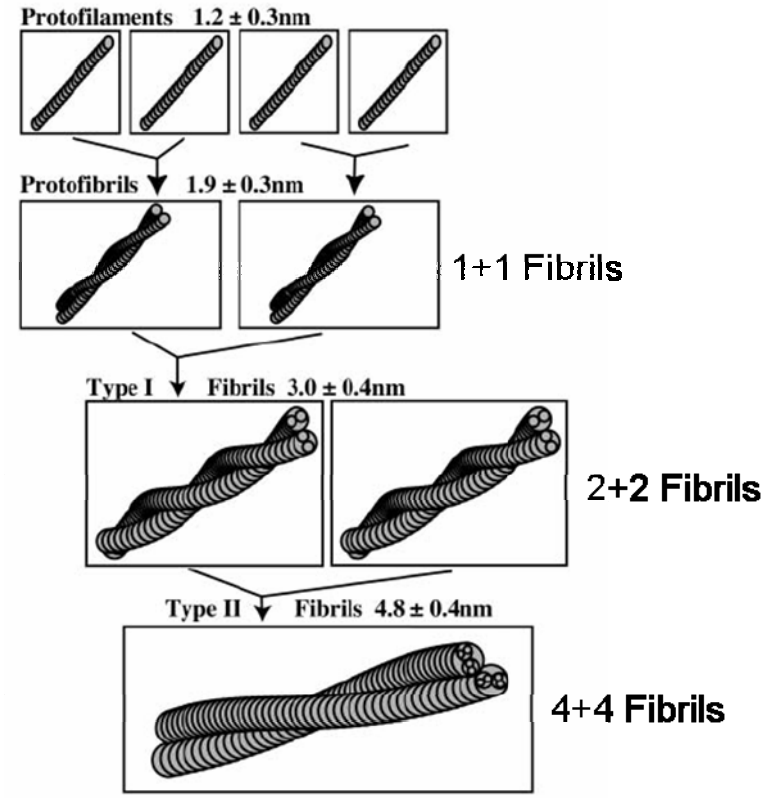

Figure 3-19 A model for the hierarchical assembly of insulin into amyloid fibrils. Protofilament pairs wind together to form "1+1" fibrils, and two "1+1" fibrils wind to form a "2+2" fibril. "4+4" fibrils are the result of winding of two "2+2" fibrils (figure adapted from Khurana 2003).

Table 3-4 The predicated heights using Khurana's model (2003).

	Protofilaments	1+1 Fibrils	2+2 Fibrils	4+4 Fibrils
Height of higher points (nm)	2.3	4.6	6.9	10.4
Height of lower points (nm)		2.3	3.4	5.2

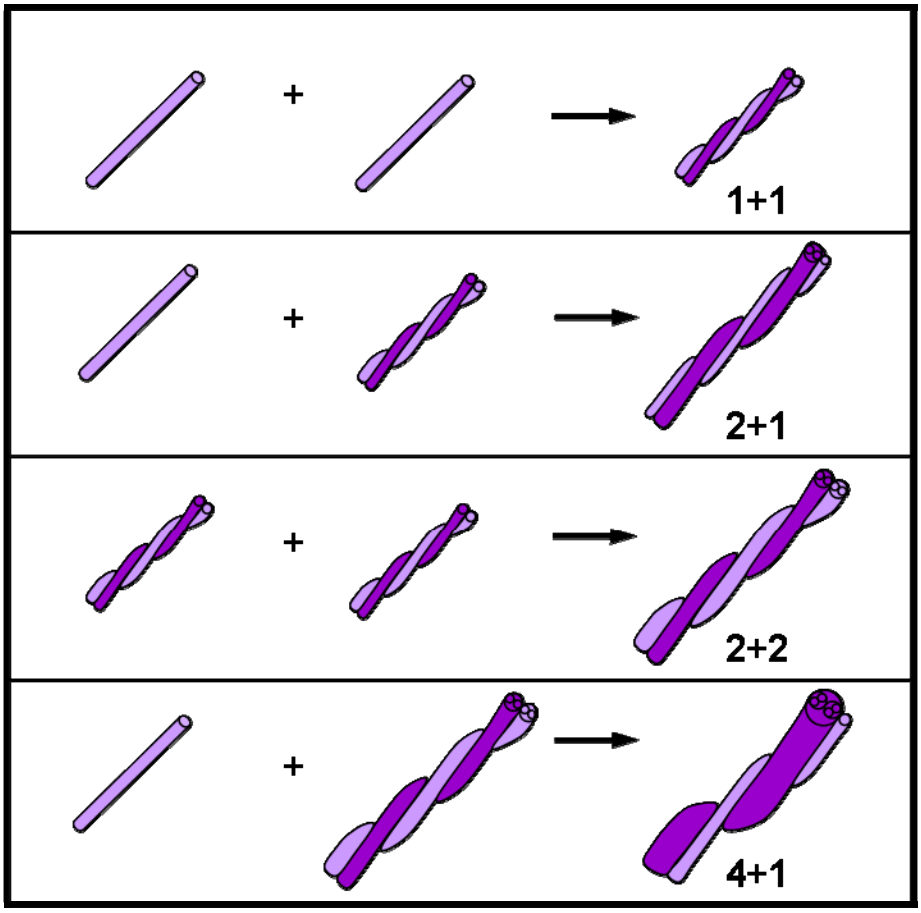

Figure 3-20 "n+1" model for lysozyme fibrils assembly. Protofilaments intertwine with each other to form "1+1" fibrils. Two "1+1" fibrils intertwine into a "2+2" fibril. A protofilament can intertwine with a "1+1" fibril to form a "2+1" fibril or with a "2+2" fibril to form a "4+1" fibril.

Table 3-5 The predicated heights using the "n+1" model.

	Protofilaments	2+1 Fibrils	4+1 Fibrils
Height of higher points (nm)	2.3	5.8	7.5
Height of lower points (nm)		3.4	5.2

Compared with **Table 3-5** with **Table 3-3**, Type III lysozyme fibrils fit well into "2+1" model, and Type V fibrils fit well into "4+1" model. The data is summed up in **Table 3-6** for comparison.

Table 3-6 The summary of the experimental data of the heights of lysozyme fibrils and the heights predicted by Khurana's model and "n+1" model.

Fibrils model		1+1	2+1	2+2	4+1	4+4
Experimental data	Average height of higher points (nm)	4.5 ± 0.3	5.7 ± 0.1	7.0 ± 0.3	7.2 ± 0.2	10.2 ± 0.2
	Average height of lower points (nm)	2.5 ± 0.2	3.8 ± 0.1	3.5 ± 0.2	5.4 ± 0.2	6.0 ± 0.1
Predicted by model	Height of higher points (nm)	4.6	5.8	6.9	7.5	10.4
	Height of lower points (nm)	2.3	3.4	3.4	5.2	5.2

Note that for the heights of the higher points, the experimental data are 4% less to 2% more than predicated by the model. However, for the heights of the lower points, the experimental data are 3% to 15% more than predicated by the model; especially for the "4+4" fibrils, the experimental data is ((6.0-5.2) / 5.2 =) 15% more than predicated by the model. This might be because the fibrils were raised from the mica surface at the lower points due to the stiffness of the fibrils and intertwining, which would increase the height of the lower points measured from the profile of AFM images. Since the stiffness increased with the increasing of the assembly level (a detailed discussion of the elasticity of the lysozyme fibrils will

be presented in section **4.3**), the increasing of the height of the lower points of "4+4" fibrils was more observable than other fibrils.

Using both Khurana's model and "n+1" model, the fibrils observed on AFM images can therefore be explained. An example is given in **Figure 3-21**: a "1+1" fibril intertwines with a protofilaments to form a "2+1" fibril.

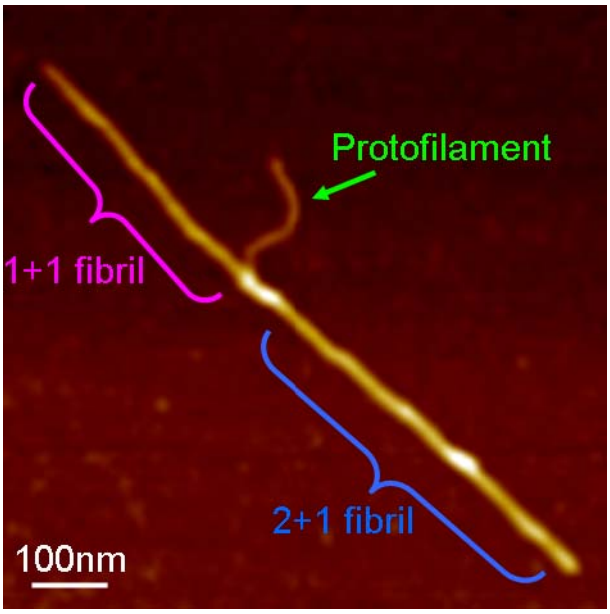

Figure 3-21 An AFM height image of a lysozyme fibril after 4 days of incubation. The fibril indicated by green arrow has height of 2.4 ± 0.1 nm, which could be a protofilament; the fibril indicated by pink bracket has average height of higher points 4.6 ± 0.1 nm and lower points 2.8 ± 0.1 nm, which could be a "1+1" fibril; the fibril indicated by the blue bracket has an average height of higher points 5.5 ± 0.5 nm and lower points 3.5 ± 0.1 nm, which could be a "2+1" fibril. The Z-range is 9.1 nm.

Some fibrils were observed to be connected to more than one fibril (**Figure 3-18**), suggesting that the formation of mature fibrils from the intertwining of subunits

might happen starting from the two ends or even in the middle of the subunits; also that fibrils of different assembly levels might be forming at the same time.

3.2.4 The Late Stages of Lysozyme Fibrillization

After 11 to 14 days of incubation (**Figure 3-22**), the sample solution started to have a gel-like appearance. Most lysozyme fibrils appeared to have clear periodicity with a periodicity to diameter ratio of ~20. Interestingly, some fibrils appeared to have sinusoidal shape (**Figure 3-22**, indicated by pink arrows), which might be due to some degree of unwinding of the subunits created during the adsorption process of the fibrils to the substrate.

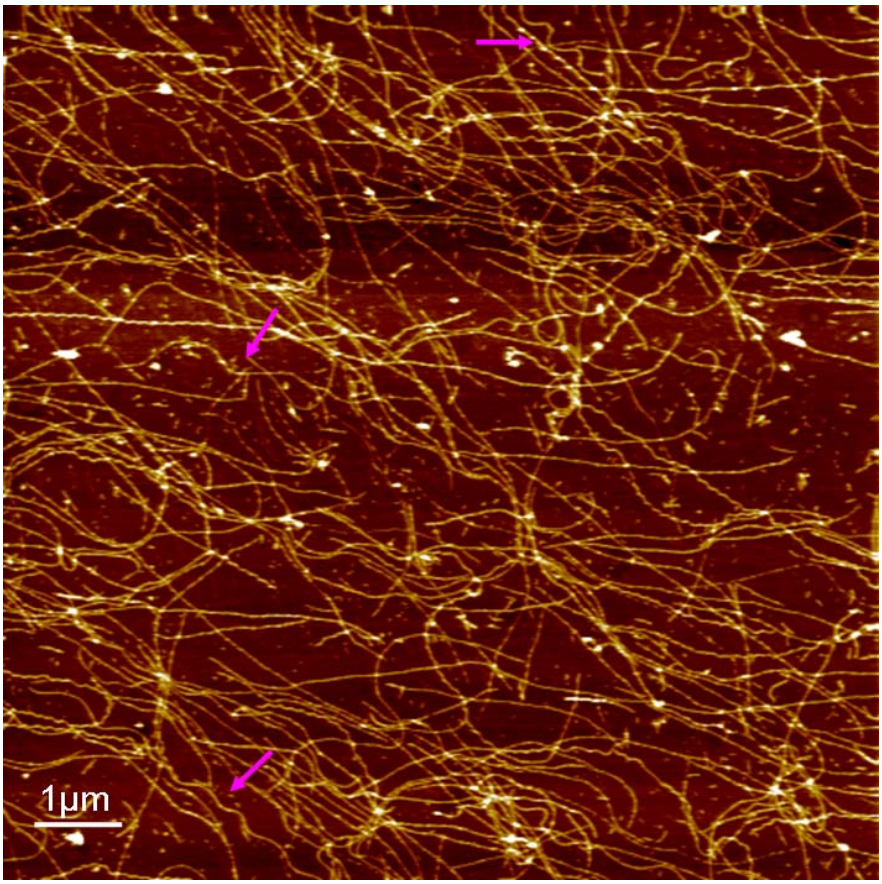

Figure 3-22 An AFM height image of lysozyme fibrils after 11 days of incubation. The pink arrows indicate some fibrils with sinusoidal shape. The Z-range is 26.6 nm.

Circular fibrils, the diameter of which was typically 250~350 nm, were also observed after 14 days of incubation (**Figure 3-23**).

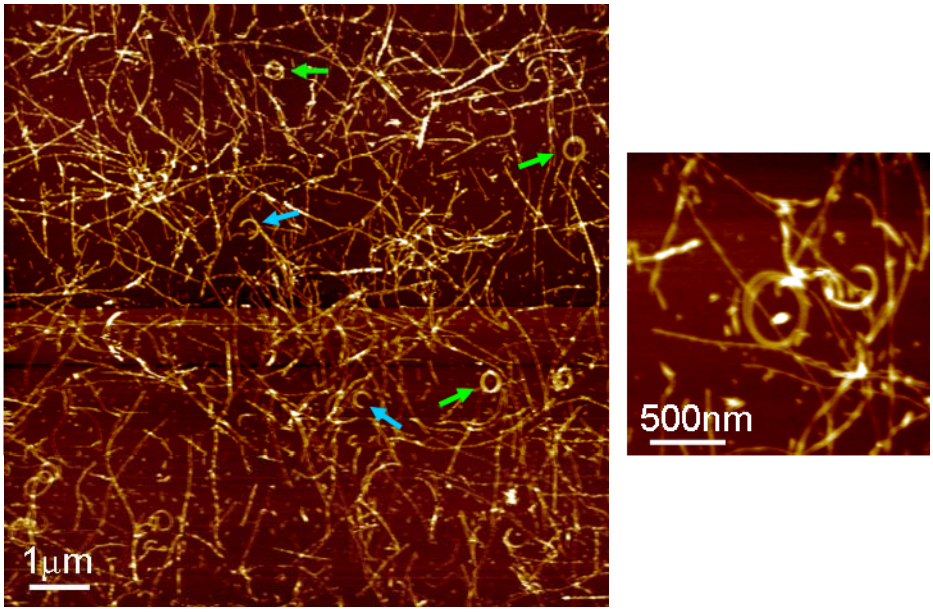

Figure 3-23 AFM height images of lysozyme fibrils after 14 days of incubation. The green arrows indicate several fibrils with circular structures. The blue arrows indicate two fibrils with half circular structures. The image on the right has better resolution, with one circular fibril on the middle. The Z-range of the left image is 24.3 nm.

Previous studies on solvational and hyperbaric tuning of amyloidogenesis with insulin fibrils suggested that circular structures of amyloid fibrils are probably a lower void volume alternative to straight fibrils (Jansen *et al.* 2004; Grudzielanek *et al.* 2005; also see section **1.3.1.3**). The fact that the circular structure of lysozyme fibrils were only observed at the late stages of fibrillization when fibrils became "crowded", agreed with this theory. However, no high hydrostatic pressure and addition of cosolvents or cosolutes were required in this case, which

suggests that simpler conditions could be applied to manipulate the conformation of amyloid fibrils.

3.3 Alternative Assembly of Tubular and Spherical Nanostructures from FF Peptides

The self-assembly of FF peptide monomers into nanotubes happens very rapidly (Reches and Gazit 2003). In order to observe the formation of FF nanotubes, the sample for AFM operation needs therefore to be prepared immediately after the FF nanotubes are formed, so that further self-assembly is interrupted.

FF nanotubes prepared by Reches and Gazit's method (2003), where FF peptide was dissolved in HFIP at high concentrations (100mg/mL) and then diluted into the aqueous solution at a final μM concentration range (for detailed preparation see section **2.2.4**), were typically several micrometers in length and 50 to 300 nm in diameter (**Figure 3-24**). However, short and thin fibrillar structures of 2 to 4 nm in height were also sometimes observed along with the long and thick nanotubes (**Figure 3-24**). Associating with the tentative model proposed by Görbitz (2006) (see section **1.3.3.2**), the long and thick nanotubes may have their proposed multilayer tubular wall, while the short and thin fibrils might well be single-wall nanotubes.

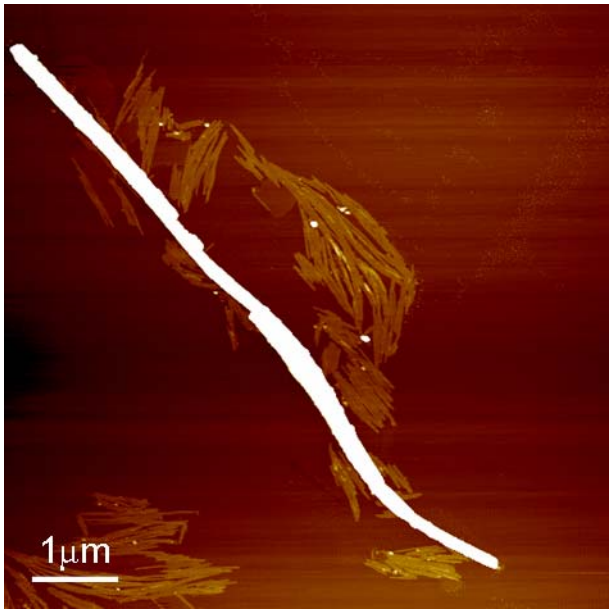

Figure 3-24 AFM image of typical long and thick FF nanotubes along with short and thin fibrilar structures. The long and thick FF nanotubes lying from the top left to the bottom right on the middle of this image is whitened because the colour scale has been adjusted in order to enhance the appearance of the short and thin fibrilar structures. The Z-range is 107.2 nm.

Song and co-workers reported (2004) another nanotube preparation method, where FF peptide was dissolved in water to 2mg/mL at 65 °C, and the sample equilibrated for 30 min and then gradually cooled to room temperature (**Figure 3-25** a). They noted that when 0.1 mL of the nanotube mixture was diluted by adding 0.1 mL of water, vesicles were present in addition to the nanotubes (**Figure 3-25** b; also see section **1.3.3.1**). Song suggested that the concentration of the peptide is a key factor in the formation of the nanotubes. However, by noticing the presence of vesicles in the SEM image of FF nanotubes before dilution in Song's paper (**Figure 3-25** a, indicated by pick arrows), I suspected that the temperature might play an important role in the alternative formation of tubular and spherical structures. Bearing this in mind, I used modified Reches and Gazit's (2003)

method to investigate the effect of temperature on the formation of FF nanostructures.

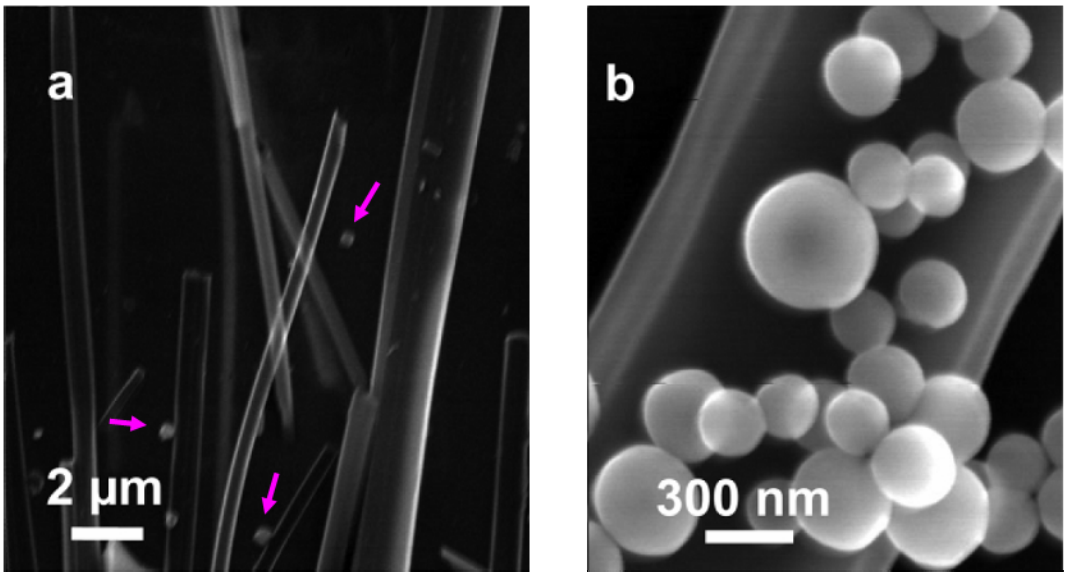

Figure 3-25 SEM images of (a) peptide nanotubes and (b) a mixture of nanotubes and vesicles (figure and caption adapted from Song *et al.* 2003, Fig 1)

FF peptide HFIP stock solution (100mg/mL) and distilled water were pre-warmed in a 40˚C water bath. The AFM sample (2mg/mL) was then prepared using this stock solutions and distilled water (detailed preparation see section **2.2.4**). An AFM topography image of this sample is displayed in **Figure 3-26**. Spherical structures of 2 to 4 nm in height were observed. Thin fibrilar structures of ~1 nm in height, 200 to 300 nm in length were also observed.

In a similar manner, the FF peptide HFIP stock solution (100mg/mL) and distilled water were pre-warmed in 65˚C water bath. The AFM sample (2mg/mL) then prepared using these stock solution and distilled water. An AFM topography

image of this sample is displayed in **Figure 3-27**. Spherical structures of 2 to 4 nm in height were observed. However, no tubular structures were observed.

As stated before, results from original Reches and Gazit's (2003) method had only nanotubes but no spherical strutures observed. Comparing the results from modified Reches and Gazit's method, it seemed that the temperature is likely to be a key factor in the alternative assembly of tubular and spherical nanostructures during FF self-assembly. The tubular structures might be kinetically favoured (Reches and Gazit 2004).

Reches and Gazit have also reported (2004) the formation of spherical nanostructures of diphenylglycine peptide, a highly similar analogue of diphenylalanine peptide. Comparing this to the formation of spherical nanostructures of FF peptides, the diphenylglycine peptide might have lower energy barrier to form spherical nanostructures. By controlling the temperature, the formation of tubular structures from diphenylglycine peptide or other analogues of FF peptide might therefore be possible.

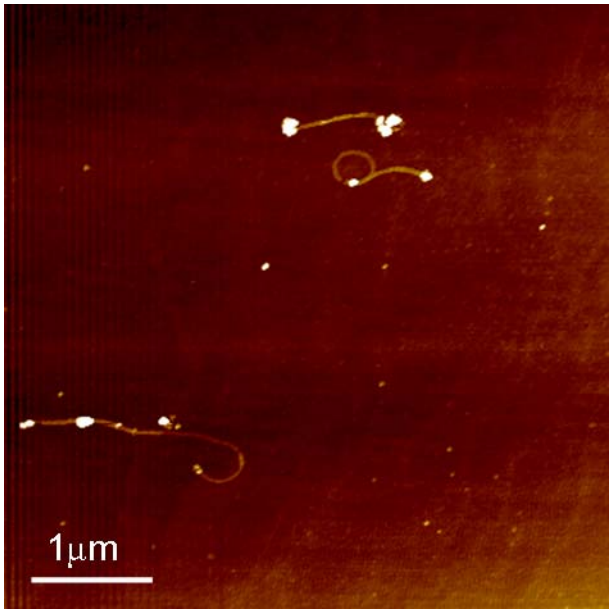

Figure 3-26 An AFM image of FF nanostructures self-assembled at 40˚C. A few thin fibrilar structures of ~1 nm in height, 200 to 300 nm in length were observed along with spherical structures of 2 to 4 nm in height. The Z-range is 21.7 nm.

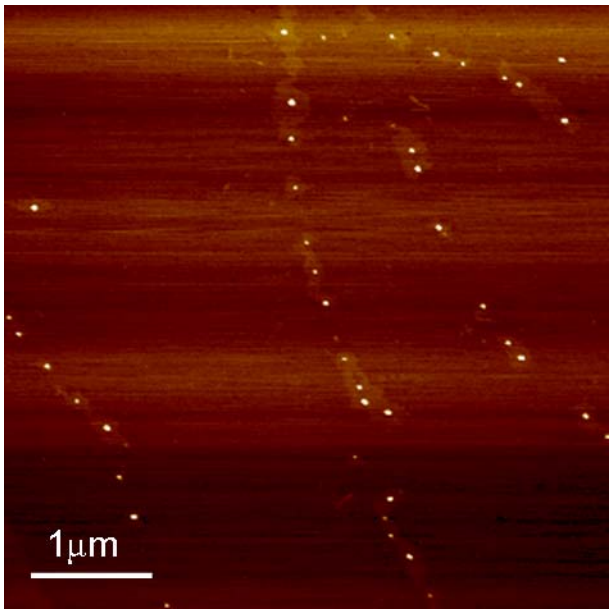

Figure 3-27 An AFM image of FF nanostructures self-assembled at 65˚C. Spherical structures of 2 to 4 nm in height were observed. The vesicles lie in lines, which is most likely due to the drying process during sample preparation. The Z-range is 6.2 nm.

3.4 Conclusion

In this chapter, the imaging capability of AFM has been explored and a range of imaging studies monitoring the dynamic processes of protein nanotubes have been presented. A better understanding of the dynamic processes of protein nanotubes, provides the information on manipulating these protein nanotubular materials, which is desired in order to utilize them in applications.

The dissociation process of *Salmonella* flagellar filaments in low pH solution was found to happen within an hour; therefore, real-time monitoring was possible. All parts of a filament exposed to the low pH solution were found to instantly break down to single flagellin proteins at the same time.

If the dynamic process of protein nanotubes occurs on timescales that are too long or too short for real-time AFM monitoring, the process has to be interrupted so that the sample can be prepared for AFM operation. For example, the fibrillization process of lysozyme fibrils takes up to two weeks, while the formation of nanostructures from FF peptides takes only a few seconds to a few minutes.

By observing the fibrillization process of lysozyme fibrils, the “n+1” model has been proposed: a protofilament may intertwine with a fibril consisting of more than one protofilament to form higher assembly level fibrils. This model complements the hierarchical assembly model proposed by Khurana (2003).

The effect of temperature on the alternative formation of tubular and spherical nanostructures of FF peptides was also investigated, which may suggest a general way of controlling the formation of nanostructures from FF peptides and its similar analogues.